Supplementary Information for

Phase-separation physics underlies new theory for the resilience of patchy ecosystems

Koen Siteur, Quan-Xing Liu, Vivi Rottschafer, Tjisse van der Heide, Max Rietkerk, Arjen Doelman, Christoffer Bostrom, and Johan van de Koppel

Corresponding Q.-X.L. or J.v.d.K
E-mail: liuqx315@gmail.com (Q.X.L.) or johan.van.de.koppel@nioz.nl (J.v.d.K.)

This PDF file includes:

Other supplementary materials for this manuscript include the following:

Movies S1 to S3

Supporting Information Text

Contents

S1. Phase separation in conservative reaction-diffusion models

Here we further elucidate the generic conceptual framework of phase separation with conservative reaction-diffusion models proposed in the main context (Eqs. 1, called *phase separation model*). The

class of models considered in this paper are of the form:

$$\frac{\partial U}{\partial T} = F(U,V) + D_U\left(\frac{\partial^2 U}{\partial X^2} + \frac{\partial^2 U}{\partial Y^2}\right) \quad \text{[S1.1a]}$$

$$\frac{\partial V}{\partial T} = G(U,V) + D_V\left(\frac{\partial^2 V}{\partial X^2} + \frac{\partial^2 V}{\partial Y^2}\right), \quad \text{[S1.1b]}$$

where U and V are state variables, T is time, X and Y represent space (with unit $[L]$),$F(U,V)$ and $G(U,V)$ are reaction terms that describe the local dynamics of the system (with unit $[U][T]^{-1}$), and D_U and D_V are diffusion rates that control the rate exchange of U and V in space (with unit $[L]^2[T]^{-1}$).

For the conservative systems discussed in the main text, matter (e.g. nutrients, sediment, grazers) is conserved locally. This means that any inflows (outflows) of U are outflows (inflows) of V. Hence,

$$G(U,V) = -CF(U,V) \quad \text{[S1.2]}$$

with C being a positive constant converting U into V (with unit $[V][U]^{-1}$).

S2. Scaling of the models

We apply the following scaling relations to obtain the dimensionless model given below

$$\begin{aligned} v &= C^{-1} \times V \\ u &= U \\ t &= T \\ f(u,v) &= F(U, C^{-1}V) \\ g(u,v) &= C^{-1}G(U, C^{-1}V) \\ x &= D_V^{-1/2} \times X \\ y &= D_V^{-1/2} \times Y \\ \delta &= D_V^{-1} \times D_U. \end{aligned}$$

Introducing this into system (S1.1) results in

$$\frac{\partial u}{\partial t} = f(u,v) + \delta\left(\frac{\partial^2 u}{\partial x^2} + \frac{\partial^2 u}{\partial y^2}\right) \quad \text{[S2.1a]}$$

$$\frac{\partial v}{\partial t} = g(u,v) + \frac{\partial^2 v}{\partial x^2} + \frac{\partial^2 v}{\partial y^2}. \quad \text{[S2.1b]}$$

For the conservative systems, as given in Eq.(2) in the main text, we have that

$$g(u,v) = -f(u,v), \quad \text{[S2.2]}$$

which gives in

$$\frac{\partial u}{\partial t} = f(u,v) + \delta\left(\frac{\partial^2 u}{\partial x^2} + \frac{\partial^2 u}{\partial y^2}\right) \quad \text{[S2.3a]}$$

$$\frac{\partial v}{\partial t} = -f(u,v) + \frac{\partial^2 v}{\partial x^2} + \frac{\partial^2 v}{\partial y^2}. \quad \text{[S2.3b]}$$

These are the systems we analyse in the following sections.

S3. Phase-plane analysis of the model

We will study the solutions of the model in absence of diffusion in subsection S3.1, before continuing with the full model in subsection S3.3.

For clarity we illustrate our analysis by choosing that the function f has a N-shaped form with $f(0,0) = 0$ and the vector field points away from both of the axes such that u and v will remain positive (see Fig. S1).

S3.1. Dynamics of the model in absence of diffusion. First, we study the solutions of conserved system (S2.3) in absence of diffusion by using phase-plane analysis, see also Refs. (1–3).

In absence of diffusion, the dynamics of the system (S2.3) is described by:

$$\frac{du}{dt} = f(u,v) \qquad \text{[S3.1a]}$$

$$\frac{dv}{dt} = -f(u,v). \qquad \text{[S3.1b]}$$

By adding and integrating, it follows that at all times:

$$u + v = \tau \qquad \text{for any time,} \qquad \text{[S3.2]}$$

where τ is a constant that reflects the total density of the species. The fact that $u + v$ is constant, constrains the dynamics of the system to the diagonal lines shown in the phase plane of Fig. S1.

The system is in equilibrium when $\frac{du}{dt} = \frac{dv}{dt} = 0$, which is the case on the nullcline

$$f(u,v) = 0.$$

Moreover, the nullclines of both equations of the system coincide and this means that there exists a line of fixed points $(\bar{u}, \bar{v})$ where $f(\bar{u}, \bar{v}) = 0$.

The black curve in Fig. S1 depicts the combinations of u and v for which the system is in equilibrium. For a given density of the model (S2.3) at initial states (equivalent the parameter τ of mobile species), the equilibrium densities u and v are given by the intersection of $v(u) = \tau - u$ and solutions of $f(\bar{u}, \bar{v}) = 0$ (here $(\bar{u}, \bar{v}) := \{(u_-, v_-), (u_0, v_0), (u_+, v_+)\}$).

In subsection S3.2 we analyse the stability of these fixed points and find that a homogeneous solution is stable when

$$f_u - f_v < 0, \qquad \text{[S3.3]}$$

or similarly when

$$\left.\frac{dv(u)}{du}\right|_{f(\bar{u},\bar{v})=0} > -1. \qquad \text{[S3.4]}$$

This results in behaviour on the line $u+v=\tau$ with movement towards the fixed point if the nullcline has a slope larger -1 and otherwise solutions move away.

The choice of the density τ is important for the resulting solutions. There exist two bifurcation points, denoted by τ_- and τ_+, where the number of fixed points change (see Fig. S1 for the intercept of formula $v=\tau-u$). When $\tau_- < \tau < \tau_+$, there exist three fixed points and for $\tau < \tau_-$ and $\tau > \tau_+$, there is only one fixed point (which is stable). Therefore, changing τ can result in a sudden shift in the densities of u and v. If we assume that the system is in the left state and that $\tau_- < \tau < \tau_+$ and then increase τ such that it hits τ_+, the system jumps from the left state to the right state (since this is the only one left).

Hence, gradual changes in the density of the species τ, can cause the system to slowly move along the nullcline and then lead to a sudden shift in the densities of u and v.

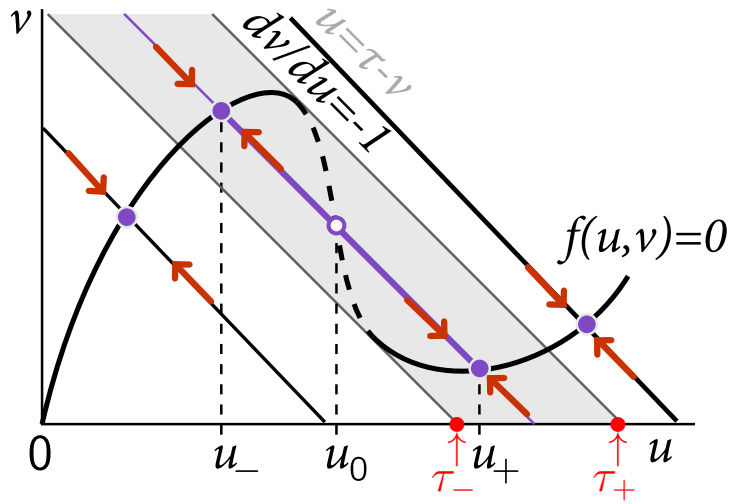

Fig. S1. Phase plane of the model (S3.1), in absence of diffusion. The dynamics of the system must lie on $u+v=\tau$, and is thus constrained to the diagonal blue lines. The nullcline (black) is given by $f(u,v)=0$. On the nullcline the system is in equilibrium meaning that neither u nor v change over time. Note that the N-shaped nullcline was chosen for clarity, but that it can take any shape (e.g. see Refs. (1–3)).

In order to study the patterns that are formed by adding diffusion, we assume that there exists a fixed point that is marginally stable in absence of diffusion, and hence, we assume that Eq. (S3.3) or Eq. (S3.4) holds in the rest of this document.

S3.2. Stability conditions in absence of diffusion. In this section we study the stability of solutions of system (S2.3) in absence of diffusion so in system (S3.1). In Section S3.1 we showed that for system (S3.1) there exists a curve of fixed points $(\bar{u},\bar{v})$.

Linearising the system around these steady states $(\bar{u},\bar{v})$ gives the Jacobian matrix

$$J(\bar{u},\bar{v}) = \begin{pmatrix} f_u & f_v \\ -f_u & -f_v \end{pmatrix}, \qquad [S3.5]$$

where $f_u = \frac{\partial f}{\partial u}|_{(\bar{u},\bar{v})}$ and $f_v = \frac{\partial f}{\partial v}|_{(\bar{u},\bar{v})}$. We determine the characteristic polynomial of $J(\bar{u},\bar{v})$ as

$$\lambda^2 - \lambda(f_u - f_v) = 0,$$

and therefore, the eigenvalues are $\lambda = 0$ and $\lambda = f_u - f_v$. The steady states of system (S3.1) are linearly marginally stable when both eigenvalues are not positive, and thus, when

$$f_u - f_v < 0. \qquad \text{[S3.6]}$$

In order to study the patterns that are formed by adding diffusion, we assume that there exists a fixed point that is marginally stable in absence of diffusion, and hence, we assume that Eq. (S3.3) (i.e. Eq. (S3.6)) always holds. This results in the following possibilities for the signs of the elements of the Jacobian (S3.5):

$$\begin{pmatrix} + & + \\ - & - \end{pmatrix}, \quad \begin{pmatrix} - & - \\ + & + \end{pmatrix}, \quad \begin{pmatrix} - & + \\ + & - \end{pmatrix}. \qquad \text{[S3.7]}$$

Moreover, condition (S3.3) can be related to the slope of the nullcline $f(u,v) = 0$. Upon differentating the expression of the nullcline with respect to u we obtain $f_u + \frac{dv}{du} f_v = 0$, and hence $\frac{dv}{du} = -\frac{f_u}{f_v}$. Thus, by combining this with $f_u < f_v$ we find that the fixed point $(\bar{u},\bar{v})$ is stable when $\frac{dv}{du}|_{f(u,v)=0} > -1$.

S3.3. Dynamics of the model including diffusion: The diffusive instability. Besides instability of the homogeneous (constant) solutions as discussed in the previous sections, these homogeneous solutions can also become unstable when adding diffusion to the equations (in case the homogeneous solution is stable without diffusion) Then, spatial patterns form out of the spatially uniform steady states studied in the previous section.

This instability belongs to a class of Turing/diffusive instabilities that are referred as Type II-instabilities (4, 5). In section S3.4 we show that patterns are formed out of the homogeneous state when

$$f_u - \delta f_v > 0, \qquad \text{[S3.8]}$$

and similarly when the slope of the nullcline gets below $-\delta$, i.e. when

$$-\delta > \left.\frac{dv(u)}{du}\right|_{f(u,v)=0} > -1, \qquad \text{[S3.9]}$$

see also see Refs.(1, 2). This corresponds to the region highlighted in Fig. S2.

Summarizing, patterns are formed when

$$f_u - f_v < 0 \qquad \text{[S3.10a]}$$
$$f_u - \delta f_v > 0. \qquad \text{[S3.10b]}$$

Thus, it follows that we must assume $\delta \neq 1$ in order to obtain patterns.

Moreover, we show in subsection S3.4 that the patterns that are formed have a wavenumber that lies close to the critical wavenumber $k_c = 0$, so they have small wave numbers, hence, this resuls in large-scale patterns. In practice this means that patches that are formed at the onset of pattern formation lie further apart in conserved systems than the patches in Turing systems.

In non-conservative reaction diffusion models, equivalent conditions to the above are given by

$$f_u + g_v < 0 \quad \text{[S3.11a]}$$
$$f_u g_v - f_v g_u > 0, \quad \text{[S3.11b]}$$

for stability of the constant state without diffusion, and

$$f_u g_v - f_v g_u > 0 \quad \text{[S3.12a]}$$
$$(f_u + \delta g_v)^2 > 4\delta(f_u g_v - f_v g_u), \quad \text{[S3.12b]}$$

for a diffusive instability. In that instability, spatially periodic patterns bifurcate.

Moreover, the critical wavenumber around which patterns are formed is

$$k_c^2 = \frac{f_u g_v - f_v g_u}{d}. \quad \text{[S3.13]}$$

Note that, for conserved systems the size of the diffusion constant is determined by the sign of f_u. Namely, if $f_u > 0$ then by the first condition ($f_u < f_v$) also $f_v > 0$ and by the second condition ($f_u > f_v\delta$) $\delta < 1$. Now assume $f_u < 0$ then f_v must also be negative and $\delta > 1$. Thus in order to have diffusive instability there are two possibilities for the signs of the terms in the Jacobian:

$$\begin{pmatrix} + & + \\ - & - \end{pmatrix}, \quad \begin{pmatrix} - & - \\ + & + \end{pmatrix}. \quad \text{[S3.14]}$$

Hence, we can deduce that conservative systems belong to the activator-depleted substrate.

From this condition we can conclude that for conservative systems (S2.3):

For $\delta < 1$ and changing τ starting with a value $\tau_- < \tau < \tau_+$, periodic patterns are formed before the stable homogeneous solution disappears in case which the solution would shift to another pattern.

Note that here τ should be $\langle\tau\rangle = \frac{1}{\Omega}\int_\Omega (u+v)dxdy$ for spatial diffusion systems.

The total density at which such pattern forming instability occurs is referred to as τ_T and τ_D in the main text, and borders the so-called (in physics) spinodal region, depicted in Fig. 5 of the main text.

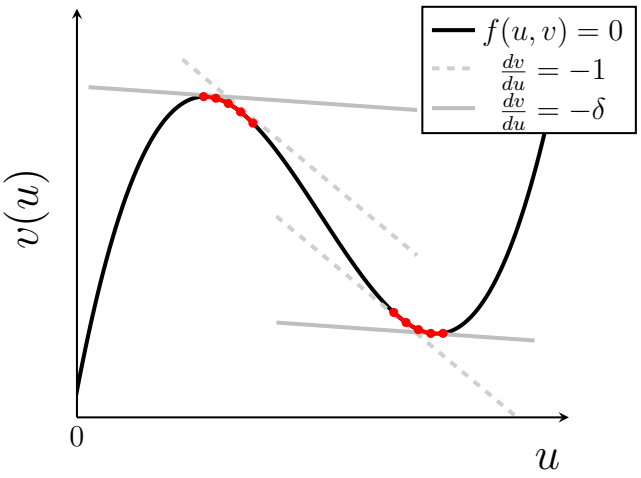

Fig. S2. Plot of the nullcline $f(u,v)=0$ and the regions (red dots) where patterns occur for $0<\delta<1$.

S3.4. Linear stability analysis of the full system. Next, we study the conditions for pattern formation when diffusion is present. This gives further restrictions on the possibilities of signs of the elements of the Jacobian. Note that to simplify theoretical analyses, we adopt the one-dimensional space instead of the two-dimension scenario in the following, but the conclusions are valid to the generic two-dimensional spatial model (S2.3). Upon substituting

$$\begin{aligned} u &= \bar{u}+\tilde{u}e^{ikx+\lambda t}, \\ v &= \bar{v}+\tilde{v}e^{ikx+\lambda t}, \end{aligned}$$

with $k\in\mathbf{R};\lambda\in\mathbf{C}$, into system (S2.3) and linearising, we obtain the linear eigenvalue problem,

$$\lambda\begin{pmatrix}\tilde{u}\\ \tilde{v}\end{pmatrix}=\begin{pmatrix}f_u-\delta k^2 & f_v\\ -f_u & -f_v-k^2\end{pmatrix}\begin{pmatrix}\tilde{u}\\ \tilde{v}\end{pmatrix}=A\begin{pmatrix}\tilde{u}\\ \tilde{v}\end{pmatrix}. \qquad [S3.15]$$

Note that the case $k=0$ corresponds to the system without diffusion. The characteristic polynomial corresponding to (S3.15) is given by

$$\lambda^2+\lambda(f_v-f_u+k^2(\delta+1))+k^2(\delta f_v-f_u)+\delta k^4=0; \qquad [S3.16]$$

and therefore, the eigenvalues are given by

$$\lambda_\pm=\frac{1}{2}\Big(\mathrm{tr}(A)\pm\sqrt{\mathrm{tr}(A)^2-4\mathrm{det}(A)}\Big),$$

with $\mathrm{tr}(A)=f_u-f_v-k^2(\delta+1)$ and $\det(A)=k^2(\delta f_v-f_u+\delta k^2)$. Figure S3B shows qualitatively different plots of the eigenvalues as function of the wave numbers.

Note that at $k=0$, one of the eigenvalues is always zero. In the case when $f_u-f_v<0$, $\lambda_+(k=0)=0$. Moreover, close to $k=0$, the eigenvalues are always real. And, when $\delta<1$ and $f_u+f_v<0$, the eigenvalues are real for every k.

Next, we determine the critical wave number k_c which is the first wavenumber for which solutions of system (3) (main text) become unstable. Since $\mathrm{Re}(\lambda_+)\geq\mathrm{Re}(\lambda_-)$, we can focus on the branch

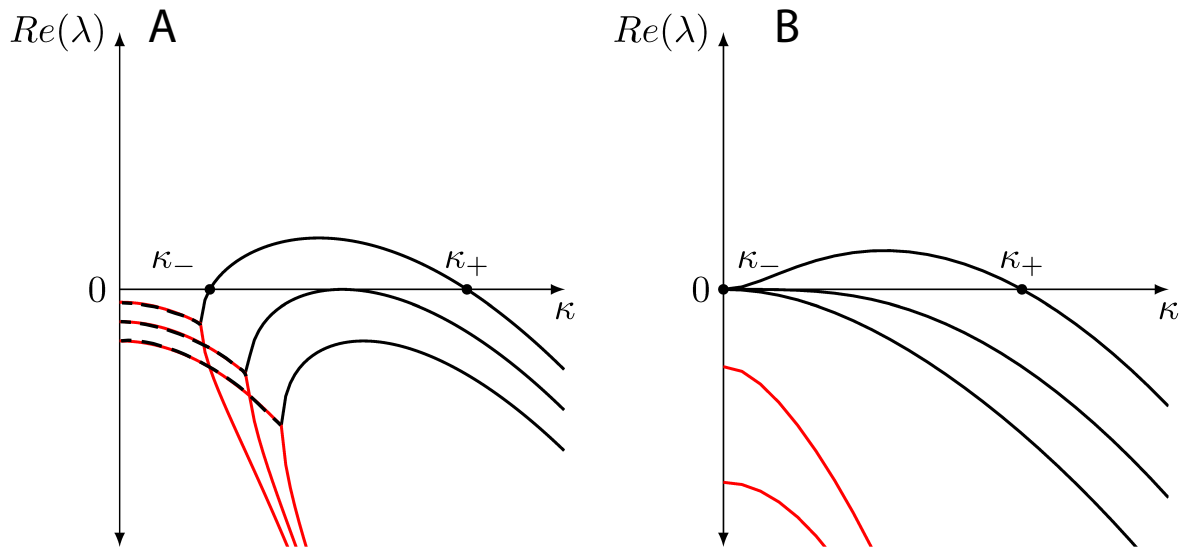

Fig. S3. Amplitude growth rates (Eq. (S3.16)) as a function of perturbation wavenumber for (A) non-conservative and (B) conservative systems, with λ_+ in black and λ_- in red. Environmental change was simulated by changing f_u with $\delta < 1$.

$\mathrm{Re}(\lambda_+)$ and find that the critical wave number is equal to zero, $k_c = 0$.
To see this, we first assume that the eigenvalues are real. Then, at the critical wave number $k = k_c$, both $\lambda_+ = 0$ and $\frac{\partial \lambda_+}{\partial k} = 0$ must hold. Differentiating (S3.16) with respect to k and using these conditions we find that

$$2k_c(\delta f_v - f_u) + \delta k_c^3 = 0.$$

This leads to solutions $k_c = 0$ or $k_c^2 = \frac{f_u - f_v\delta}{2\delta}$ where the latter only exists when $f_u - f_v\delta \geq 0$. Moreover, using that $\lambda = 0$ at $k = k_c$, we find that k_c must satisfy the relation

$$k_c^2(f_v\delta - f_u) + \delta k_c^4 = 0. \qquad [S3.17]$$

The choice $k = 0$ is always a solution to this equation. Then substituting of $k_c^2 = \frac{f_u - f_v\delta}{2\delta}$ into (S3.17) results in $-\frac{f_u - f_v\delta}{2\delta} = 0$. Thus, when $f_u - f_v\delta = 0$ the eigenvalue curve also touches the axis for this value of k_c, leading to a fourth order curve close to $k = 0$. When $f_u - f_v\delta \neq 0$, $k_c^2 = \frac{f_u - f_v\delta}{2\delta}$ does not satisfy (S3.17). Therefore, a bifurcation takes place when $f_u - f_v\delta = 0$ when the eigenvalue curve $\lambda_+(k)$ transforms from having a maximum at $k = 0$ for $f_u - f_v\delta < 0$ to having a minimum at $k = 0$ and maxima at $k^2 = \frac{f_u - f_v\delta}{2\delta}$ that lie above the axis, see Fig. S3B. So, the wave numbers close to zero are the first to become unstable.

Next, when assuming that the eigenvalues are complex, we find that

$$\mathrm{Re}\lambda_\pm = \frac{1}{2}\Big(\mathrm{tr}(A) = \frac{1}{2}(f_u - f_v - k^2(\delta + 1)\Big),$$

such that $k = 0$ is also the first wavenumber to become unstable. In Fig. S3B, we plot both eigenvalues for $\delta > 1$ and $f_u < 0$, and $f_v < 0$. So that the eigenvalues are real and the imaginary part of λ is always zero. We change f_u so that first $f_u - f_v\delta < 0$ holds and the curves lie below the axis. Then we increase f_u so that $f_u - f_v\delta > 0$ and there exists a range of k-values where one of the eigenvalues is positive.

The condition $f_v\delta < f_u < f_v$ (for which patterns are formed) can also be rewritten in terms of the slope of the nullcline $f(u,v) = 0$. Similar as in Section S3.2 we find that patterns arise when $-1 < \frac{dv}{du}|_{f(u,v)=0} < -\delta$.

S3.5. Required feedbacks for pattern formation. In this section we first summarise conditions for pattern formation for general non-conservative systems (S2.1). Following the reasoning of Segel and Jackson (6, 1972) and Edelstein-Keshet (7, 1988), conditions Eqs. (S3.11) and (S3.12) have the following implications on pattern formation:

1. *Coefficients f_u and g_v have contrasting signs.* The signs of these coefficients determine whether state variables u and v self-enhance (positive) their growth or hamper it (negative). If f_u is positive (and g_v negative), then u is referred to as the activator. In the following f_u is taken positive.

2. *Coefficients f_v and g_u have contrasting signs.* These coefficients determine the interactions between the state variables. If f_u is positive and g_v negative, then v has a negative effect on activator u, while activator u stimulates the growth of v. These systems are referred to as activator-inhibitor systems (see Fig. S4A). If f_v is positive and g_u negative, then v has a positive effect on activator u, while activator u depletes v. These systems are referred to as activator-depleted substrate systems (see Fig. S4B).

3. *The range of diffusion of the activator u is smaller than that of the inhibitor/substrate v:* $\sqrt{\delta/|f_u|} < \sqrt{1/|g_v|}$. In an activator-inhibitor system this allows inhibitor that is produced in a patch of activator to diffuse out of it. In activator-depleted substrate systems it implies that substrate between activator patches can diffuse into the patches.

To understand the types of feedbacks that result in pattern formation in non-conservative ecosystems, let us consider two scenarios:

1. Matter (e.g. carbon or water) flows through the system from a slowly diffusing state u to a rapidly diffusing state v.

2. Matter flows through the system from a rapidly diffusing state v to a slowly diffusing state u.

Figure S5 depicts neutral models of these two systems, in which the outflow from u and v is proportional to the levels of u and v (e.g. linear-reservoirs). Observe that these neutral models are not able to reproduce patterns, but that in scenario 1 (Fig. S5A) an increase in u leads to an increase in v (i.e. $g_u > 0$), which corresponds to the activator-inhibitor class, and that in scenario 2 (Fig. S5B) an increase in v leads to an increase in u (i.e. $f_v > 0$), which corresponds to the activator-depleted substrate class.

In Figure 2 of the main text, the dashed arrows represent additional feedbacks that are required to explain pattern formation in both scenarios. The feedbacks depicted in Fig. 2A are typical for systems where u represents plants and v plant litter (e.g. van de Koppel and Crain (8)). The

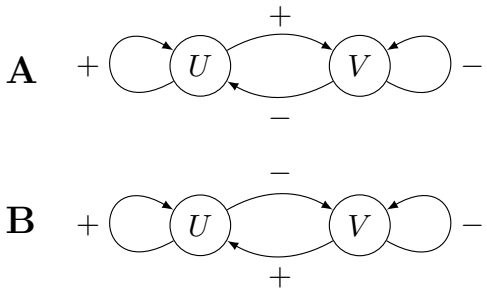

Fig. S4. (A) Activator-inhibitor interactions (positive f_u and g_u, and negative f_v and g_v) and (B) activator-depleted substrate interactions (positive f_u and f_v and negative $g_u U$ and g_v).

feedbacks depicted in Fig. 2B are typical for systems where u represents consumers and v represents a limiting resource (e.g. see Refs. (10, 29)).

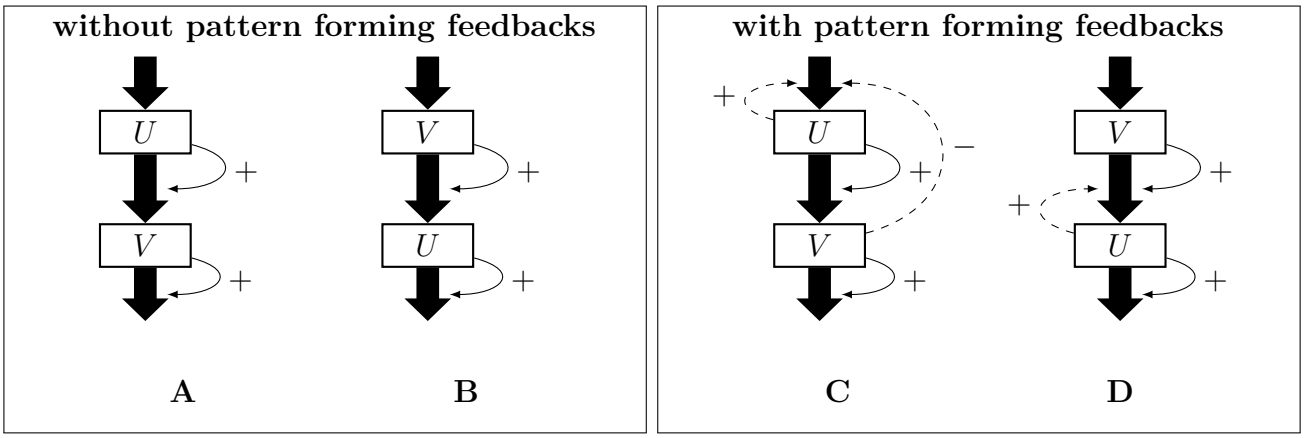

Fig. S5. Both activation-inhibition feedbacks and activation-depletion feedbacks can be responsible for patterning in ecosystems where pattern formation involves a through-flow of resources. *Left*, The left panel shows null-models, without pattern forming feedbacks. *Right*, The right panel shows possible ways by which pattern forming feedbacks can be introduced (dashed lines). Here (C) captures the feedbacks in the freshwater marshes studied by van de Koppel and Crain (8) with U (u, in dimensionless model S2.1) being marsh vegetation and V (v, in dimensionless model S2.1) wrack, and (D) corresponds with feedbacks found in arid ecosystems (11), with V representing surface water and U soil water.

S3.6. Required feedbacks for pattern formation in conservative systems. Now that we have established that conservative systems belong to the activator-depleted substrate class, with the activator u diffusing faster than the substrate v , we can think about the types of feedbacks required for pattern formation in conservative systems. If matter switches randomly between u and v, as in the neutral model depicted in Figs. S6 and S5C, D, then an increase in v leads to a greater flow from v to u, meaning that $f_v > 0$ and $g_v < 0$, which is in line with the activator-depleted substrate interactions (Fig. S4A). However, the flow from u to v increases with u, resulting in $f_u < 0$ and $g_u > 0$, meaning that the neutral model cannot explain patterns in closed systems.

For pattern formation we require $f_u > 0$ and $g_u < 0$. There are three ways to accomplish this:

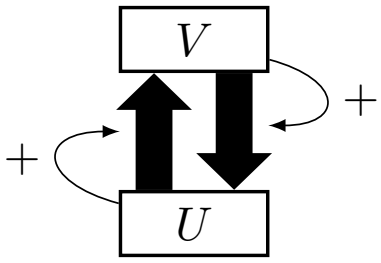

Fig. S6. Neutral model for conservative systems.

1. U reduces its outflow (dashed arrow 1 in Figure 2 of the main text)
2. U increases its inflow (dashed arrow 2 in Figure 2 of the main text)
3. a combination of scenario 1 and scenario 2.

Notice that U may increase/reduce its in-/outflow through some ecosystem engineer, as described in the main text and Table 1. Examples of 2 are the models model by Mori et al. (12) and Samuelson et al. (3).

S4. Pattern solutions, and the binodal region

It is worthy of note that the analytical construction of the solutions given in this section is only valid in 1 dimension. Our numerical simulations suggest that the solutions of model in 2D are similar to those in 1D.

In this section, we study stationary patterns by setting $\frac{\partial u}{\partial t} = \frac{\partial v}{\partial t} = 0$. Substitution of this into system (S2.3) gives

$$\begin{aligned} 0 &= f(u,v) + \delta \frac{\partial^2 u}{\partial x^2} \\ 0 &= -f(u,v) + \frac{\partial^2 v}{\partial x^2}. \end{aligned} \qquad [S4.1]$$

Adding these two equations yields:

$$\delta \frac{\partial^2 u}{\partial x^2} + \frac{\partial^2 v}{\partial x^2} = 0. \qquad [S4.2]$$

Upon assuming that patterns remain bounded, it follows from equation Eq. (S4.2) that

$$\delta u + v = r, \qquad [S4.3]$$

where r is a priori unknown constant, but for our systems here it depends on the total density of species.

Pattern solutions obey Eq. (S4.3), meaning that densities of u and v may vary in space, but yet lay on a straight line through the phase plane, as depicted by the blue line in Fig. S7.

Notice that from Eq. (S4.1) it follows that u and v have no curvature at $f(u,v)=0$ (i.e. the 2nd derivative is zero). The densities of u and v at the locations of zero curvature are therefore given by intersections of the black line and the blue line in Fig. S7.

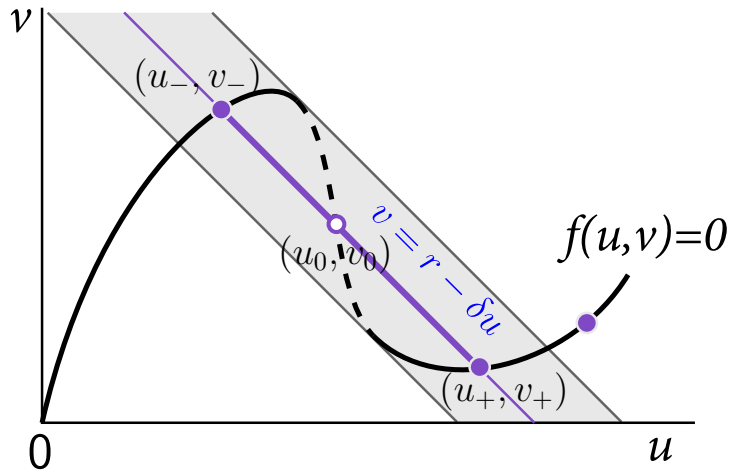

Fig. S7. Phase plane of the model. Pattern solutions of the system must satisfy $\delta u + v = r$, and thus lay on the black lines. On the blue line $f(u,v)=0$ and both u and v have zero curvature in space.

In order to study solutions that arise we introduce two new variables:

$$r = \delta u + v, \quad s = \delta u - v,$$

see also Ref. (13). The system (S4.1) then becomes

$$\begin{aligned} \tfrac{\partial^2 r}{\partial x^2} &= 0 \\ \tfrac{\partial^2 s}{\partial x^2} &= -2f(\tfrac{1}{2\delta}(s+r), \tfrac{1}{2}(r-s)) := -g(s,r) \end{aligned}$$

Because of the boundary conditions r becomes constant. We now denote r by $\bar{r}$ which is a constant. Then, the system reduces to

$$\frac{\partial^2 s}{\partial x^2} = -g\,(s, \bar{r}) \qquad \text{[S4.4]}$$

In the 1-dimensional setting, we analyse the phase plane of Eq.(S4.4) by looking at the fixed points, see also ref. (13) for the more detailed explanation. These solutions of $g\,(s,\bar{r})=0$ correspond to intersections of the line $\delta u + v = \bar{r}$ and $f(u,v)=0$ as depicted in Fig. S7 by the intersection of the black line and blue curve.

In order for patterns to occur we must choose the value of $\bar{r}$ such that there are three intersections: two intersections that approximate the maxima and minima of the pattern solution (indicated by $+$ and $-$ respectively), and one other intersection (see Fig. S7). We denote the solutions of $g\,(s,\bar{r})=0$ by s_0 and $s_\pm$ where $s_- < s_O < s_+$.

The equation (S4.4) for s is a Hamiltonian system (it conserves energy) with Hamiltonian given by

$$H(s,\bar{r}) = \frac{1}{2}\left(\frac{ds}{dx}\right)^2 + 2\int g\,(z,\bar{r})\,dz.$$

To construct solutions, we use energy arguments where values of s that correspond to the minima of the potential $V\,(s,\bar{r}) = \int g\,(z,\bar{r})\,dz$ represent equilibria that may be spatially stable. The Maxwell point (13–15) corresponds to the fixed points s_- and s_+ having the same Hamiltonian. So, we need to choose $\bar{r}$ such that

$$H(s_-,\bar{r}) = H(s_+,\bar{r}).$$

Then the system is said to be at Maxwell point Hence, for a this choice of $\bar{r}$ $(= r^*)$ a stationary solution connecting the one state s_- to the other s_+ exists; this is a so-called front solution. This is related to the fact that the areas under the function g must be the same, see Fig. S8 for a specific case in this study.

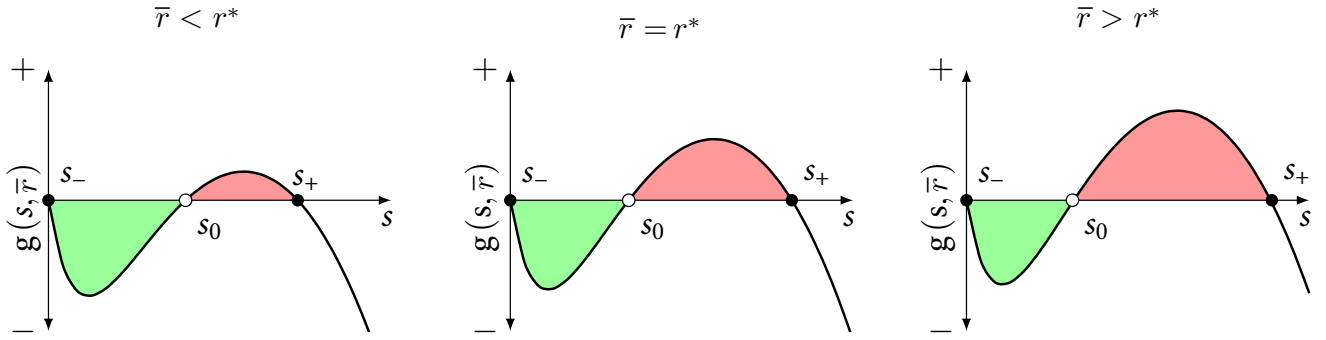

Fig. S8. Visualization of the Maxwell point where the areas under the function f must be the same.

In the main text we have established that the cover of the +-state is a function of the spatially averaged density of the mobile species:

$$c(\langle\tau\rangle) \approx \frac{\langle\tau\rangle - \tau_-}{\tau_+ - \tau_-},$$

where c is the cover of the +-state, with $0 \leq c \leq 1$. τ is the sum of local u and v, and $\langle\rangle$ indicates the spatial average. This implies that pattern solutions can only exist within the range:

$$\tau_- < \langle\tau\rangle < \tau_+ \qquad [S4.5]$$

The region where both the uniform steady state is stable, i.e. outside the spinodal region bordered by τ_T (and τ_D) (where condition S3.9 is violated), and patterns exist (where condition S4.5 is met), is referred to as the binodal region in the main text (see Fig. 5).

Given that pattern solutions lay on the line $v(u) = \bar{r} - \delta u$, which has a slope of $-\delta$ and at least three intersections with the line $f(u,v) = 0$, we can deduce that pattern solutions exist beyond both sides of the spinodal region. In other words, the spinodal region lays within the pattern existence

region (Eq. (S4.5)). From this we can conclude that:

The spinodal region, defined by lateral instability, is bordered by a binodal region, that is characterised by the coexistence of a patterned and a stable spatially uniform steady state.

S5. The aggregation-dissipation model

With the slightly rescaled parameters on our original models, three different aggregation-dissipation models can be written to a general model (S2.1). The aggregation-dissipation model mentioned in the main text is a conservative reaction-diffusion model, as studied in section S3 and S4, but with specified reaction terms:

$$\frac{\partial u}{\partial t} = vu - \frac{\alpha}{\beta + u}u + \delta\left(\frac{\partial^2 u}{\partial x^2} + \frac{\partial^2 u}{\partial y^2}\right) \quad \text{[S5.1a]}$$

$$\frac{\partial v}{\partial t} = \frac{\alpha}{\beta + u}u - vu + \left(\frac{\partial^2 v}{\partial x^2} + \frac{\partial^2 v}{\partial y^2}\right). \quad \text{[S5.1b]}$$

The model captures both feedbacks 1 and 2 depicted in Fig. 2B and D (maintext), which are relevant in oligotrophic systems, grazing systems, and biogeomorphological systems. We describe models for these three systems, which can all be scaled to Eq. (S2.1). Table S1 shows how the scaled parameters and variables of Eq. (S2.1) relate to the parameters and variables of the models, and lists the values that were used to obtain the figures in the main text.

S5.1. Nutrient recycling. In oligotrophic environments, where plant growth is nutrient limited, plants take up nutrients during growth and release them again when they die and decompose. This can be represented by:

$$\frac{\partial P}{\partial T} = G(N)P - D(P)P + D_P\left(\frac{\partial^2 P}{\partial X^2} + \frac{\partial^2 P}{\partial Y^2}\right) \quad \text{[S5.2a]}$$

$$\frac{\partial N}{\partial T} = c_4 D(P)P - c_4 G(N)P + D_N\left(\frac{\partial^2 N}{\partial X^2} + \frac{\partial^2 N}{\partial Y^2}\right), \quad \text{[S5.2b]}$$

here P represents the plant density and N the nutrient concentration in the water/soil column. The plant growth rate is a linear function of the nutrient concentration:

$$G(N) = c_1 N.$$

The plant death rate decreases with plant density due to facilitation:

$$D(P) = \frac{c_2}{c_3 + P}.$$

At a plant density of $P = 0$ the death rate is c_2/c_3 and at a density of $P = c_3$ the death rate is reduced by 50%. Nutrients are released during plant death and taken up again during plant growth.

Parameter c_4 is a conversion constant, converting P into N. The diffusion terms represent the clonal dispersion of plants and the lateral flow of nutrients through the soil/water column, where the former process generally occurs over much longer timescales: $D_P \ll D_N$.

Notice that in absence of diffusion, i.e. if P and N are uniformly distributed or if D_P and D_N are zero, then Eq. (S5.2) simplifies to a model studied graphically by Noy-Meir (1975, 16) and May (1977, 17), since:

$$\frac{dN}{dT} = -c_4 \frac{dP}{dT} \quad [S5.3]$$

$$\int dN = -c_4 \int dP \quad [S5.4]$$

$$N = N_0 - c_4 P. \quad [S5.5]$$

Here N_0 is the concentration of N in absence of P. Substituting in Eq. (S5.2a) gives:

$$\frac{dP}{dT} = c_1(N_0 - c_4 P)P - \frac{c_2}{c_3 + P}P \quad [S5.6]$$

which is often written as:

$$\frac{dP}{dT} = r\left(1 - \frac{P}{K}\right)P - \frac{c_2}{c_3 + P}P \quad [S5.7]$$

with $r = c_1 N_0$ and $K = N_0/c_4$.

Table S1. Physical meaning of parameters and variables in the model and their (initial) values.

scaled model	nutrient recycling	picky grazing	sediment trapping	(initial) value
α	c_2	$c_8^{-1} \times c_6 c_9$	$c_{13}^{-1} \times c_{11}$	4
β	$c_1^{\frac{1}{2}} c_4^{\frac{1}{2}} \times c_3$	$c_5^{\frac{1}{2}} c_9^{\frac{1}{2}} c_8^{-\frac{1}{2}} \times c_7$	$c_{10}^{\frac{1}{2}} c_{14}^{\frac{1}{2}} c_{13}^{-\frac{1}{2}} \times c_{12}$	1
δ	$D_N^{-1} \times D_P$	$D_m^{-1} \times D_g$	$D_s^{-1} \times D_d$	$[0.25, 0.625, 0.01]$
u	$c_1^{\frac{1}{2}} c_4^{\frac{1}{2}} \times P$	$c_5^{\frac{1}{2}} c_8^{\frac{1}{2}} c_9^{-\frac{1}{2}} \times H_g$	$c_{10}^{\frac{1}{2}} c_{13}^{\frac{1}{2}} c_{14}^{\frac{1}{2}} \times S_d$	$[\sqrt{\alpha} - \beta, ..., \sqrt{\alpha/\delta} - \beta]$
v	$c_1^{\frac{1}{2}} c_4^{-\frac{1}{2}} \times N$	$c_5^{\frac{1}{2}} c_8^{\frac{1}{2}} c_9^{-\frac{1}{2}} \times H_f$	$c_{10}^{\frac{1}{2}} c_{13}^{\frac{1}{2}} c_{14}^{-\frac{1}{2}} \times S_s$	$[\sqrt{\alpha}, ..., \sqrt{\alpha\delta}]$
t	$c_1^{\frac{1}{2}} c_4^{\frac{1}{2}} \times T$	$c_5^{\frac{1}{2}} c_8^{\frac{1}{2}} c_9^{-\frac{1}{2}} \times T$	$c_{10}^{\frac{1}{2}} c_{13}^{\frac{1}{2}} c_{14}^{\frac{1}{2}} \times T$	$[0, ..., 2500]$
x	$c_1^{\frac{1}{4}} c_4^{\frac{1}{4}} D_N^{-\frac{1}{2}} \times X$	$c_5^{\frac{1}{4}} c_8^{\frac{1}{4}} c_9^{-\frac{1}{4}} D_f^{-\frac{1}{4}} \times X$	$c_{10}^{\frac{1}{4}} c_{13}^{\frac{1}{4}} c_{14}^{\frac{1}{4}} D_s^{-\frac{1}{4}} \times X$	$[0, ..., 100]$
y	$c_1^{\frac{1}{4}} c_4^{\frac{1}{4}} D_N^{-\frac{1}{2}} \times Y$	$c_5^{\frac{1}{4}} c_8^{\frac{1}{4}} c_9^{-\frac{1}{4}} D_f^{-\frac{1}{4}} \times Y$	$c_{10}^{\frac{1}{4}} c_{13}^{\frac{1}{4}} c_{14}^{\frac{1}{4}} D_s^{-\frac{1}{4}} \times Y$	$[0, ..., 100]$

S5.2. Picky grazing. Herbivore behaviour is largely determined by the spatial distribution of available forage. Here we adopt a binary description of herbivore behaviour from van de Koppel et al. (18) and divide herbivores into grazing and foraging herbivores that switch between these two activities depending on available forage.

$$\frac{\partial H_g}{\partial T} = S_{fg}(F)H_f - S_{gf}(F)H_g + D_g\left(\frac{\partial^2 H_g}{\partial X^2} + \frac{\partial^2 H_g}{\partial Y^2}\right) \quad [S5.8a]$$

$$\frac{\partial H_f}{\partial T} = S_{gf}(F)H_g - S_{fg}(F)H_f + D_f\left(\frac{\partial^2 H_f}{\partial X^2} + \frac{\partial^2 H_f}{\partial Y^2}\right). \quad [S5.8b]$$

The rate at which herbivores stop foraging and start grazing is proportional to the fraction of available forage F:

$$S_{fg}(F) = c_5 F(P).$$

In contrast, the rate at which herbivores switch from grazing to foraging decreases with the fraction of available forage F:

$$S_{gf}(F) = \frac{c_6}{c_7 + F(P)}.$$

Where $S_{gf}(0) = c_6/c_7$ is the rate at which herbivores switch to foraging in absence of available forage. If $F = c_7$, then the rate of switching to foraging is halved.

The fraction of available forage is assumed to decrease linearly to zero as plant density P approaches the carrying capacity K, due to decreasing palatability at high biomass:

$$F(P) = 1 - \frac{P(H_g)}{K}.$$

With logistic plant growth and proportional grazing, plant biomass asymptotically approaches:

$$P(H_g) = K\left(1 - \frac{c_8}{c_9} H_g\right),$$

where c_8 is the grazing rate and c_9 is the growth rate of plants.

The movement of grazing and foraging herbivores is modelled through ordinary diffusion. Given that herbivores are free to switch between grazing and foraging, their resulting movement pattern obeys composite brownian motion (if $D_g \neq D_f$), which is in agreement with observations (19).

Notice that we relax the assumption by van de Koppel et al. (18) that herbivores can move is instantaneously to any location in the modelled domain. In this model, this scenario would be approximated by selecting a high diffusion rate of foraging herbivores D_f. We take the movement of herbivores to be finite, although naturally $D_f \gg D_g$.

S5.3. Sediment trapping. In biogeomorphological systems sediment is either in a deposited state or in a suspended/aeolian state. The theoretical model can be expressed as follows:

$$\frac{\partial S_d}{\partial T} = D(P)S_s - E(P)S_d + D_d\left(\frac{\partial^2 S_d}{\partial X^2} + \frac{\partial^2 S_d}{\partial Y^2}\right) \quad [S5.9a]$$

$$\frac{\partial S_s}{\partial T} = c_{14}E(P)S_d - c_{14}D(P)S_s + D_s\left(\frac{\partial^2 S_s}{\partial X^2} + \frac{\partial^2 S_s}{\partial Y^2}\right). \quad [S5.9b]$$

Here, S_s is the concentration of suspended/aeolian sediment, S_d is the height of plant trapped sediment, and c_{14} converts S_d into S_s.

The deposition rate $D(P)$, i.e. the rate at which suspended/aeolian sediment is trapped, is assumed to be proportional to the plant biomass:

$$D(P) = c_{10}P(S_d). \quad [S5.10]$$

The rate at which deposited sediment erodes decreases with plant density following:

$$E(P) = \frac{c_{11}}{c_{12} + P(S_d)}. \quad [S5.11]$$

Where the erosion rate in absence of plants is given by $E(0) = c_{11}/c_{12}$. At a plant density of $P = c_{12}$ the bare soil erosion rate is halved. The plant density is assumed to increase linearly with the height of deposited sediment:

$$P(S_d) = c_{13} S_d. \quad [S5.12]$$

S5.4. Stability and pattern formation in the aggregation-dissipation model (S5.1). In this section the stability of the steady states of Eq. (S5.1) is determined using the conditions derived in section S3 and section S4 to plot bifurcation Fig. 5 in main text. In this analysis we assume that $u, v \geq 0$.

The spatially uniform steady states of Eq. (S5.1) can be found by assuming no change over time $\frac{\partial u}{\partial t} = \frac{\partial v}{\partial t} = 0$ and space $\frac{\partial^2 u}{\partial x^2} = \frac{\partial^2 v}{\partial x^2} = 0$ and $\frac{\partial^2 u}{\partial y^2} = \frac{\partial^2 v}{\partial y^2} = 0$:

$$vu = \frac{\alpha}{\beta + u} u. \quad [S5.13]$$

This equation has two solutions, $(\bar{u}_0, \bar{v}_0)$ and $(\bar{u}, \bar{v})$, located on the lines

$$\bar{u}_0 = 0 \quad [S5.14]$$

$$\bar{v}(\bar{u}) = \frac{\alpha}{\beta + \bar{u}} \quad [S5.15]$$

plotted in Fig. S9.

As discussed in section S3, the steady states of conservative systems are either neutrally stable or unstable. In subsection S3.2 we found that, in absence of diffusion, a steady state is neutrally stable when

$$f_u \leq f_v. \quad [S5.16]$$

These derivatives are given by:

$$f_u(u, v) = v - \frac{\alpha\beta}{(\beta + u)^2} \quad [S5.17]$$

$$f_v(u, v) = u. \quad [S5.18]$$

Then, we find for $(\bar{u}_0, \bar{v}_0) = (0, \bar{v}_0)$ that it is stable for

$$\bar{v}_0 \leq \frac{\alpha}{\beta}. \quad [S5.19]$$

Similarly, the other steady state $(\bar{u}, \bar{v})$, is neutrally stable if:

$$\bar{u} \geq \sqrt{\alpha} - \beta, \quad [S5.20]$$

which can be written in terms of v as:

$$\bar{v} \leq \sqrt{\alpha}. \quad [S5.21]$$

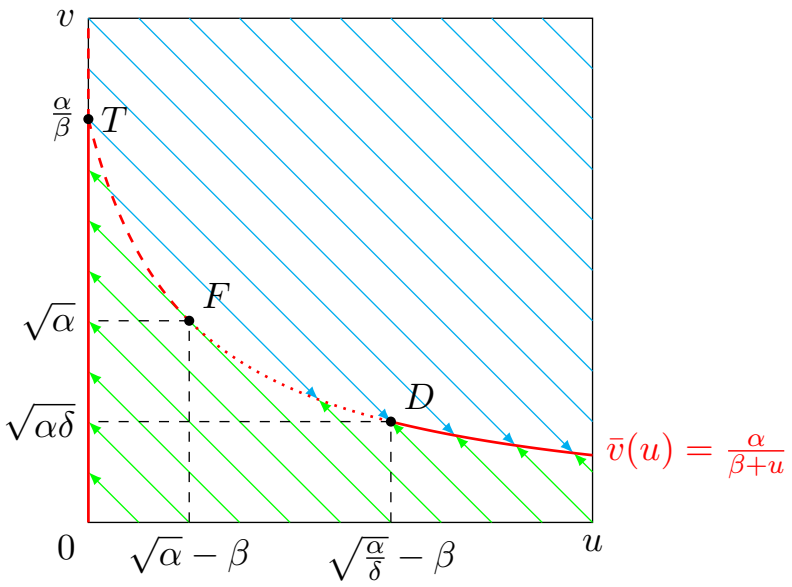

Fig. S9. Phase plane of the aggregation-dissipation model (S5.1). D marks a diffusive instability, F is a bifurcation where the steady state becomes unstable (to the left of the point it is unstable) and at T the solution $(\bar{u}, \bar{v})$ disappears. If $u + v$ is conserved in the system (constant $\langle\tau\rangle$) and if u and v are spatially uniformly distributed, then the system evolves along the diagonal arrows. The dashed and doted lines represent an unstable state, but the solid line represents a stable state.

In subsection S3.3 we showed that diffusive instability occurs if both condition Eq. (S5.16) and

$$f_u > \delta f_v, \tag{S5.22}$$

are satisfied. Under these conditions, small amplituse patterns arise. For $\bar{u}_0 = 0$ this gives:

$$\bar{v}_0 > \frac{\alpha}{\beta}. \tag{S5.23}$$

Since inequalities Eqs. (S5.19) and (S5.23) cannot both be true, no diffusive instability of $(\bar{u}_0, \bar{v}_0)$ can occur. A diffusive instability of the other steady state, $(\bar{u}, \bar{v})$ arises when

$$\bar{u} < \sqrt{\frac{\alpha}{\delta}} - \beta, \tag{S5.24}$$

which can be written in terms of v as:

$$\bar{v} > \sqrt{\alpha\delta}. \tag{S5.25}$$

We find by comparing inequalities Eqs. (S5.20) and (S5.24) that a diffusive instability can only occur if $\delta < 1$, i.e. if the diffusion of u is slower than the diffusion of v.

S6. Response of the aggregation-dissipation model to changes in global densities

In the aggregation-dissipation model (Eqs. S2.1 or S5.1) no matter is produced/destroyed locally. However, depending on boundary conditions, matter may still enter/leave the system. In section S3

and S4 it was shown that the densities of u and v determine stability and pattern formation in the aggregation-dissipation model. Hence, an important variable in this type of system is the spatially averaged density of $u+v$, hereafter referred to as spatial global density $\langle\tau\rangle$ (τ for nonspatial density, but $\langle\tau\rangle$ for spatial density):

$$\langle\tau\rangle = \langle u+v\rangle, \tag{S6.1}$$

where $\langle f(x,y)\rangle$ denotes the average of function $f(x,y)$ over the modelled domain (Ω):

$$\frac{1}{\Omega}\iint_{x,y\in\Omega} f(x,y)dxdy. \tag{S6.2}$$

In the following, we show how changes in global density $\langle\tau\rangle$ affect local densities u and v, for spatially uniform states (subsection S6.1), and patterned states (subsection S6.2). Finally, the effect of changes in $\langle\tau\rangle$ on cover are discussed (subsection S6.3).

S6.1. Local densities of spatially uniform states. If u and v are distributed uniformly over the domain, then Eq. (S6.1) becomes:

$$\langle\tau\rangle = u+v. \tag{S6.3}$$

If $\langle\tau\rangle$ is constant in time and u and v are spatially uniform, then the dynamics of Eq. (S2.1) are restricted to the diagonal lines in the phase plane of Figure S7, which are given by:

$$v(\langle\tau\rangle,u) = \langle\tau\rangle - u. \tag{S6.4}$$

Substituting Eq. (S6.4) into Eq. (S5.1a), and assuming steady state conditions ($\frac{\partial u}{\partial t}=0$) yields three uniform steady states:

$$\bar{u}_0 = 0 \tag{S6.5}$$

$$\bar{u}_\pm(\langle\tau\rangle) = \frac{1}{2}\left(\langle\tau\rangle - \beta \pm \sqrt{(\langle\tau\rangle+\beta)^2-4\alpha}\right). \tag{S6.6}$$

Substituting in Eq. (S6.4) gives the uniform steady states in terms of $\langle\tau\rangle$:

$$\bar{v}_0(\langle\tau\rangle) = \langle\tau\rangle \tag{S6.7a}$$

$$\bar{v}_\pm(\langle\tau\rangle) = \frac{1}{2}\left(\langle\tau\rangle + \beta \mp \sqrt{(\langle\tau\rangle+\beta)^2-4\alpha}\right). \tag{S6.7b}$$

The densities of u and v change as a function of $\langle\tau\rangle$ following the above steady states, as long as they are stable. Using the stability conditions derived in section S3 and the fact that $\langle\tau\rangle = u+v$ the response of the system to changes in τ can be studied (see Fig. S3).

At high global densities $\langle\tau\rangle$ the system first resides in the spatially uniform state $(\bar{u}_+,\bar{v}_+)$. As $\langle\tau\rangle$ gradually decreases, three scenarios can unfold:

1. If $\delta<1$, then patterns form through a diffusive instability $f_u(u,v) > \delta f_v(u,v)$ with $f(u,v) = vu - \frac{\alpha u}{\beta+u}$:

$$\tau_D = \sqrt{\alpha\delta} + \frac{\alpha}{\delta} - \beta.$$

2a. If $\delta \geq 1$ and $\alpha/\beta^2 > 1$, then no patterns form and a discontinuous shift from $(\bar{u}_+, \bar{v}_+)$ to $(\bar{u}_0, \bar{v}_0)$ occurs at

$$\tau_F = 2\sqrt{\alpha} - \beta,$$

which is derivated from conditions $f_u(u, v) \leq f_v(u)$ with expression of steady states (S6.7). This is a fold bifurcation, since the steady states $(\bar{u}_\pm, \bar{v}_\pm)$ vanish, as follows from Eq. (S6.6).

2b. If $\delta \geq 1$ and $\alpha/\beta^2 \leq 1$, no patterns form and a gradual transition from $(\bar{u}, \bar{v})$ to $(\bar{u}_0, \bar{v}_0)$ occurs in the form of a transcritical bifurcation T at:

$$\tau_T = \frac{\alpha}{\beta}.$$

If $\langle\tau\rangle$ gradually increases, then the system first resides in the spatially uniform state $(\bar{u}_0, \bar{v}_0)$, which becomes unstable at $\langle\tau\rangle = \tau_T$. Here, a continuous/discontinuous transition occurs towards $(\bar{u}_+, \bar{v}_+)$. If $(\bar{u}_+, \bar{v}_+)$ is unstable, that is if $\tau_D > \tau_T$, then patterns form at τ_T. This is the case if $\delta < \beta^2/\alpha$. Hence, theoretically, we can obtain the phase diagram as was shown in Fig. 5A of the main text.

The stability analysis in section S3 of the uniform states of the aggregation-dissipation model only provides insights regarding the dynamics of Eq. (S5.1) in proximity to uniform states. Analyses of the patterned state of Eq. (S5.1) are provided in subsection S6.2 and S6.3.

S6.2. Local densities of the patterned state. The aggregation-dissipation model has a patterned state consisting of two distinct uniform states coexisting in space (see Fig. 3D). This patterned state can be constructed along the same lines as in section S4 by introducing two new variables:

$$r = \delta u + v, \quad s = \delta u - v.$$

The system (S4.1) then becomes

$$\begin{aligned} \tfrac{\partial^2 r}{\partial x^2} + \tfrac{\partial^2 r}{\partial y^2} &= 0 \\ \tfrac{\partial^2 s}{\partial x^2} + \tfrac{\partial^2 s}{\partial y^2} &= -2f(\tfrac{1}{2\delta}(s+r), \tfrac{1}{2}(r-s)) := -g(s,r). \end{aligned}$$

Because of the boundary conditions r becomes constant we denote this by r^* which is a constant. Then, the system reduces to

$$\frac{\partial^2 s}{\partial x^2} + \frac{\partial^2 s}{\partial y^2} = -g\left(s, r^*\right), \qquad [S6.8]$$

where

$$g\left(s, r^*\right) = \frac{1}{4\delta}\left((r^*)^2 - s^2\right) - \frac{\alpha(s + r^*)}{2\delta\beta + s + r^*}.$$

The fixed points of this system are found by setting $\left(\frac{\partial^2 u}{\partial x^2} = \frac{\partial^2 u}{\partial y^2} = 0\right)$. This yields the following solutions:

$$s_0(r) = -r^* \qquad [S6.9]$$

$$s_\pm(r) = \pm\sqrt{(r^*)^2 + 2\delta(\beta - 2\alpha)}. \qquad [S6.10]$$

The Hamiltonian corresponding to system Eq. (S6.8) is given by

$$H(s,r^*) = \frac{1}{2}\left(\frac{ds}{dx}\right)^2 + 2\int g\,(z,r^*)\,dz \qquad \text{[S6.11]}$$

$$= \frac{1}{2}\left(\frac{ds}{dx}\right)^2 + \frac{1}{2\delta}\Big((r^*)^2 - s^3/3\Big) - 2\alpha(s-2\delta\beta)\log(2\delta\beta + s + r^*). \qquad \text{[S6.12]}$$

Table S2. Estimated values of r^* and corresponding values of $(\tilde{u}_0, \tilde{v}_0)$ and $(\tilde{u}_\pm, \tilde{v}_\pm)$ for different values of δ used in this paper.

Parameter	$\delta = 0.25$	$\delta = 0.0625$	$\delta = 0.01$
r^*	1.8543	1.0213	0.43588
$\tilde{u}_0$	0	0	0
$\tilde{v}_0$	1.8543	1.0213	0.43588
$\tilde{u}_-$	1.9001	4.3272	11.444
$\tilde{v}_-$	1.3793	0.7509	0.32143
$\tilde{u}_+$	4.5171	11.014	31.143
$\tilde{v}_+$	0.72502	0.33294	0.12444
s_0	-1.8543	-1.0213	-0.43588
s_+	0.4043	0.3554	0.1870

Then, the value of r^* for which a pattern exists, can be found by requiring that

$$H(s_0, r^*) = H(s_+, r^*). \qquad \text{[S6.13]}$$

The search for the value of r^* that satisfies Eq. (S6.13) can be interpreted as searching for the value of r for which the green and red regions in Fig. S8 have an equal area. The numerically estimated value of r^*, as well as the corresponding local densities s_0, $(\tilde{u}_0, \tilde{v}_0)$ and s_+, $(\tilde{u}_+, \tilde{v}_+)$ between which a pattern exists are given in Table S2 for different values of δ.

S6.3. Fractional cover and the existence of a patterned state. In subsection S6.1 and S6.2 we established that if u and v are spatially uniformly distributed, then local densities are governed by the global density $\langle\tau\rangle$, and that if u and v are in a patterned state, then the local densities are independent of the global density. Here we present the implications of the latter finding for the fractional cover and the existence of a patterned state.

Defining cover as the fraction of the area that resides in the $(\tilde{u}_+, \tilde{v}_+)$ phase we can approximate the relationship between the global density $\langle\tau\rangle$ and cover ratio C by two states as:

$$\langle\tau\rangle = \langle u + v\rangle \qquad \text{[S6.14a]}$$

$$\approx C(\tilde{u}_+ + \tilde{v}_+) + (1-C)(\tilde{u}_0 + \tilde{v}_0) \qquad \text{[S6.14b]}$$

for $0 \leq C \leq 1$. Bringing C to the left hand side gives:

$$C(\langle\tau\rangle) \approx \frac{\langle\tau\rangle - \tau_0}{\tau_+ - \tau_0} \quad \text{[S6.15]}$$

for $\tau_0 \leq \langle\tau\rangle \leq \tau_+$, with $\tau_+ = \tilde{u}_+ + \tilde{v}_+$ and $\tau_0 = \tilde{u}_0 + \tilde{v}_0$. This approximation is also known as the *lever rule* in general physics (20).

The above implies that changes in τ will result in a linear response in cover, and that a patterned state (an incomplete, non-zero cover) can only exist for $\tau_0 \leq \langle\tau\rangle \leq \tau_+$.

Note that u is proportional to plant density in the nutrient recycling model (subsection S5.1) and the sediment trapping model (subsection S5.3), such that the cover of $(\tilde{u}_+, \tilde{v}_+)$ state corresponds to plant cover. However, in the picky grazing model (subsection S5.2) u is proportional to the density of grazing herbivores, which negatively affect plant density. Therefore, the cover ratio C corresponds to the overgrazed, low plant density, fraction of the area in this model.

S7. Scale-dependent feedback model

The plots of Figs. **3A**, **3C** and **3E** were made using a model similar to the aggregation-dissipation model (section S5), but with the difference that now the v is replenished from an external source, rather than from u:

$$\frac{\partial u}{\partial t} = vu - \frac{\alpha}{\beta + u}u + \delta\left(\frac{\partial^2 u}{\partial x^2} + \frac{\partial^2 u}{\partial y^2}\right) \quad \text{[S7.1a]}$$

$$\frac{\partial v}{\partial t} = \gamma - v - vu + \frac{\partial^2 v}{\partial x^2} + \frac{\partial^2 v}{\partial y^2}. \quad \text{[S7.1b]}$$

The model belongs to the class of activator-depleted substrate models (subsection S3.5). Notice that the model resembles a model by van de Koppel et al. (21) albeit with a different scaling and diffusion of rather than advection of v. In this context, u would represent mussels that form patterns by competing for algae v. The algae enter the system from an upper water layer with a scaled algae concentration of γ.

The plots in Fig. 3 were made using $\alpha = 4$, $\beta = 2$, $\gamma = [2.1, \cdots, 3.5]$ and $\delta = 0.01$. The initial values of u and v were set to the steady states $\bar{u}$ and $\bar{v}$:

$$\bar{u} = \frac{\gamma\beta - \alpha}{\alpha - \gamma} \quad \text{[S7.2a]}$$

$$\bar{v} = \frac{\alpha - \gamma}{\beta - 1}. \quad \text{[S7.2b]}$$

S8. Model implementation

The aggregation-dissipation model (S5.1) and the scale-dependent feedback model (S7.1) were implemented by discretizing t, x and y. The dimensionless time t ran from 0 to 2500, with a timestep

of $\Delta t = 0.005$. Dimensionless space was implemented on a grid of 1024×1024, representing a domain of 100×100. Hence, each gridcell represents an area of $\Delta x \times \Delta y \approx 0.0977 \times 0.0977$.

The models were solved in Matlab R2016B using finite difference methods. The rates of change in u and v were calculated from forward differences and the diffusion rates of u and v were calculated using the 2nd order central differences. The grids were loaded on a graphics processing unit (Nvidia Quadro K6000) to accelerate the computations.

Periodic boundaries were used to minimize boundary effects. A uniform steady state was used as initial conditions for u and v for all model runs. For the aggregation dissipation model the steady state values of $\bar{u}$ and $\bar{v}$ are given by Eq. (S6.6) and (S6.7b) (the + state was used), and for the scale-dependent feedback model they are given by Eq. (S7.2a) and (S7.2b). To trigger pattern formation, a small amount of additive, spatially uncorrelated, normally distributed noise with a standard deviation of $\sigma = 10^{-4}$ was added to both u and v at $t = 0$.

The parameter values that were used for the model runs are given in Section S2 and Section S5. For both models, the diffusion coefficients were set to $\delta = 0.01$.

S8.1. Scale-dependent feedback plot. The scale-dependent feedback plot of Fig. 3 in maintext was obtained by calculating the cross-correlation between u and the per capita change in u at $t = 250$, between gridcells separated by a distance of $D(i,j) = \sqrt{(\Delta x \Delta i)^2 + (\Delta y \Delta j)^2}$, which is given by:

$$C(\Delta i, \Delta j) = \frac{\sum_{i=1}^{m} \sum_{j=1}^{n} [u(i,j) - \mu_u][g(i+\Delta i, j+\Delta j) - \mu_g]}{\sigma_u \sigma_g} \qquad [S8.1]$$

here i and j represent the column and row number of the $m \times n$ grid, $g(i,j) = v(i,j) - \frac{\alpha}{\beta + u(i,j)}$ is the per capita change in u, σ_u and σ_g are the standard of u and g respectively.

S8.2. Density-dependent aggregation plot. The density-dependent aggregation plot of Fig. 3 was obtained by deriving the net diffusion out of a patch of u as a function of the local density of u. We take the perspective of u, i.e. a patch is an area with high u. Since v diffuses in the opposite direction of u, the net diffusion should be calculated by subtracting the diffusion of v from the diffusion of u in model (S5.1). Assuming $\frac{\partial (u-v)}{\partial t} = 0$ yields an equation for the net diffusion:

$$\delta\left(\frac{\partial^2 u}{\partial x^2} + \frac{\partial^2 v}{\partial y^2}\right) - \left(\frac{\partial^2 v}{\partial x^2} + \frac{\partial^2 v}{\partial y^2}\right) = 2\frac{\alpha}{\beta + u}u - 2vu. \qquad [S8.2]$$

Substituting $v(u) = r^* - \delta u$ allows calculating the net diffusion as a function of u. To create Fig. 3B we used $\delta = 0.25$ and the corresponding value of r^* in Table S2.

S8.3. Patch growth and patch size distribution functions. The sizes of the patches in the model were determined using u at $t = 250$. A gridcell was said to be in a patch if $u > \tilde{u}_-$, yielding a binary matrix. The areas of patches were determined by counting the number of connected gridcells and multiplying by the area of a single gridcell $\Delta x \times \Delta y$, where connected gridcells share a Von Neumann neighbourhood, while acknowledging the periodic boundaries.

From the patch areas a_i a patch radius r_i was estimated to enable comparison with theoretical predictions: $r_i = \sqrt{\frac{a_i}{2\pi}}$. Notice that although this conversion only makes sense for circular patches, it does not affect the fit of the log-normal distribution, which best decribed the patch size distributions for the high global densities at which non-circular patches were found. This is because if a is log-normally distributed (as suggested by theory and empirical studies), then $\sqrt{a}$ is too, since $\ln(\sqrt{a}) = \ln(a)/2$. In the figures of the main text, the patch sizes were scaled by dividing by the mean of the estimated patch radius.

The patch growth was estimated analogous to the patch size, but using a grid consisting of two layers of u at $t = 200.0$ and $t = 210.0$. Using a 3D Von Neumann neighbourhood, patches were identified and selected if they were present on both layers. Patch growth was estimated by calculating the radius of a patch at $t = 200$, subtracting the radius of the same patch at $t = 210$, and dividing the result by 10.0 (time unit).

Two probability density functions were fitted to the obtained patch-size distributions. The first is the log-normal distribution, which is known to emerge as a result of nucleation and growth processes (22):

$$f(r;\mu,\sigma) = \frac{1}{r\sigma\sqrt{2\pi}} \exp\left(-\frac{(\ln r - \mu)^2}{2\sigma^2}\right).$$

The model was parametrized using the maximum likelihood estimates:

$$\hat{\mu} = \frac{1}{n}\sum_{i=1}^{n} \ln r_i \qquad \text{[S8.3]}$$

$$\hat{\sigma}^2 = \frac{1}{n}\sum_{i=1}^{n} (\ln r_i - \hat{\mu})^2. \qquad \text{[S8.4]}$$

The second model is a distribution that follows from Lifshitz-Slyozov-Wagner (LSW) theory for Ostwald ripening (23–27):

$$g(r;\mu) = \frac{4r^2}{9\mu^3}\left(\frac{3\mu}{3\mu + r}\right)^{7/3}\left(\frac{3\mu}{3\mu - 2r}\right)^{11/3} \exp\left(\frac{2r}{2r - 3\mu}\right) \qquad \text{[S8.5]}$$

for $0 < r < 3\mu/2$ and $g(r;\mu) = 0$ for $r \geq 3\mu/2$, with μ being the mean patch radius. Following Tiryakioğlu et al. (26, 27) this model was parametrized using the maximum likelihood estimate of μ, rather than the sample mean. The maximum likelihood estimate of μ is given by the solution of:

$$\frac{dL}{d\mu} = -3n + \frac{7}{3}\sum_{i=1}^{n}\frac{r_i}{3\mu + r_i} - \frac{11}{3}\sum_{i=1}^{n}\frac{2r_i}{3\mu - 2r_i} + 3\mu\sum_{i=1}^{n}\frac{2r_i}{(2r_i - 3\mu)^2} = 0. \qquad \text{[S8.6]}$$

As the global density $\langle\tau\rangle$ decreases, the modelled patch-size distributions becomes left skewed (negative skewness, see Fig. S10B). The log-normal distribution always has a positive skewness:

$$\Gamma = (e^{\hat{\sigma}^2} + 2)\sqrt{e^{\hat{\sigma}^2} - 1}$$

and is not able to reproduce the change in skewness. The LSW distribution on the other hand has a constant negative skewness:

$$\Gamma \approx -0.92002$$

which approximates the simulated skewness at low global densities.

Both models were further compared by calculating weighted AIC values (wAIC), following Wagenmakers and Farrell (28, see Fig. S10C). The wAIC can be interpreted as the probability that a distribution function is the best model, given the data and the set of candidate models.

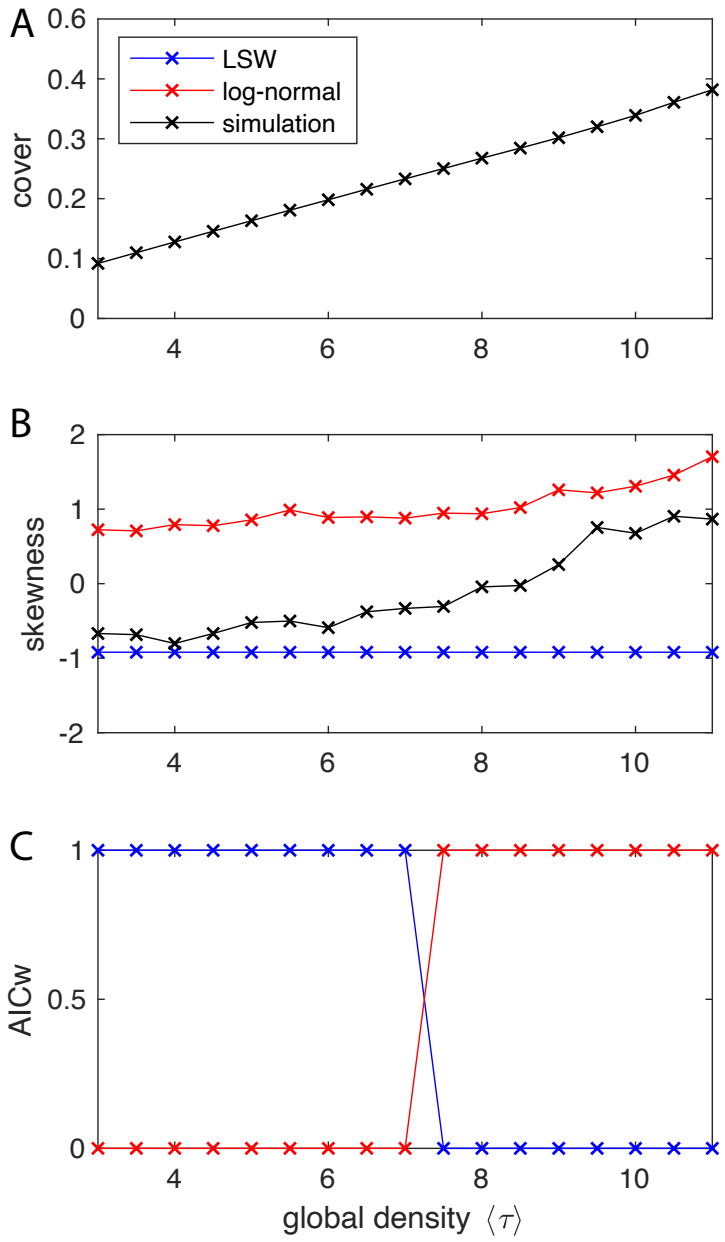

Fig. S10. Change in cover, skewness of the patch size distribution and AICw of the log-normal and LSW distributions.

S9. Comparing the global competition with scale-dependent feedbacks model

The above scale-dependent feedbacks model (S7.1) can be written as follows (Eq. (S9.7)) when we consider the plants competition water resource at global scale rather than local scales. Hence, we obtained the modified expression of this ecosystems as

$$\frac{\partial u}{\partial t} = \mathcal{G}(u,v) - \frac{\alpha u}{u+\beta} + \nabla^2 u \tag{S9.7a}$$

$$\frac{\partial v}{\partial t} = \gamma - v - \frac{1}{\Omega}\int_{\Omega} \mathcal{G}(u,v)dxdy \tag{S9.7b}$$

$$\mathcal{G}(u,v) = vu(1-u/\mathcal{K}). \tag{S9.7c}$$

Here $\mathcal{K}$ is the carrying capacity of plant communities, and Ω is the two-dimensional space for the entire area. The long-range competition leads to depleting the soil-water content in the form of $\int_{\Omega}\mathcal{G}(u,v)dxdy$. Recently, studies suggest that the patterns would appear amorphous under the global-competition scenarios, where patches spanning a wide range of sizes/areas and lacking a characteristic length scale, named as the "scale-free patterns" (30). However, the scale-dependent feedbacks patterns and proposed phase-separation patterns here show the nearly periodic patterns that have characteristic length scales, such as bands on hill slopes or spotted patterns (see Figs. 3C-D and 5C in the main text). Similarly, our competition model also reveals a scale-free pattern as were shown in Fig. S11. Note that phase-separation patterns are still spatial periodic but coarsening of their characteristic length scales with time going (see Fig. S12). The metrics of average power spectra density display the distinct dominant peaks (Figs. S12B) for the scale-dependent feedbacks model and phase-separation model independent of the varied biomass.

Overall, proposal phase-separation model here is essential different from the global competition model (Eq. (S9.7)). The radial spectrum density and patch size distribution on phase separation patterns are distinct behavior from the global competition and scale-dependent feedback model.

S10. Coarsening behavior of phase separation principle

Moreover, for the phase-separation principle (Model 3 in the main text), scaling coarsening laws is expected in spatial wavelength among patchiness on previous studies of the classical Cahn-Hilliard model, ecosystems (32), and sorted patterned ground (31). Indeed, after an initial transient, the average mesa patterns wavelength will increase with time, $\ell \propto t^{\kappa}$. One obtains a logarithmic coarsening law for all mesa patterns in a two-dimensional density-dependent aggregation (DDA) model, which yields power-law scaling with the universal exponent of 0.28 Fig.S12A. For this scaling exponent closer to 1/3, it is in excellent agreement with the standard phase-separation theory by scaling arguments, sometimes also called Lifshitz–Slyozov (LS) law (26, 27). On the contrary, the wavelength of the scale-dependent feedbacks (SDFs) model displays a slight fluctuation around constant values, which implies the spatial periodic patterns with a specific characteristic scale. We measure the spatial spectrum density starting from a randomly initialized distribution evolve into a self-organized spatial pattern. As shown in Fig.S12B, our simulations can generate the characteristic scale on both scale-dependent feedbacks (SDFs) and (DDA) density-dependent aggregation models, respectively. The dominant peak moves into large wavelengths with time going.

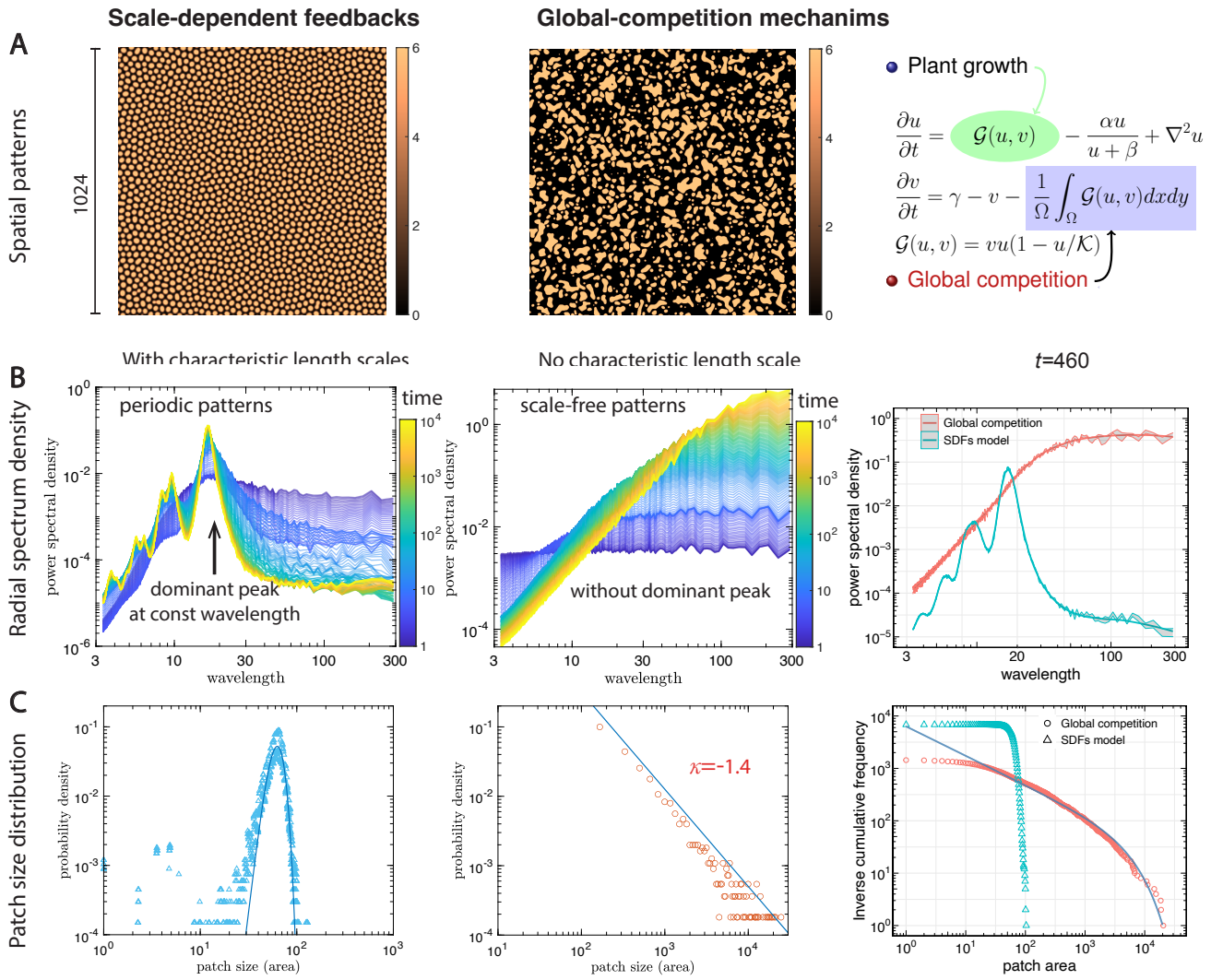

Fig. S11. Comparison of statistical properties between the scale-dependent feedback Eq. (S7.1) and its global-competition model. (A) Spatial patterns and the mathematical description of global competition mechanisms. (B) Radial spectrum density of spatial patterns on two different mechanisms. (C) Patch-size distribution of spatial patterns.

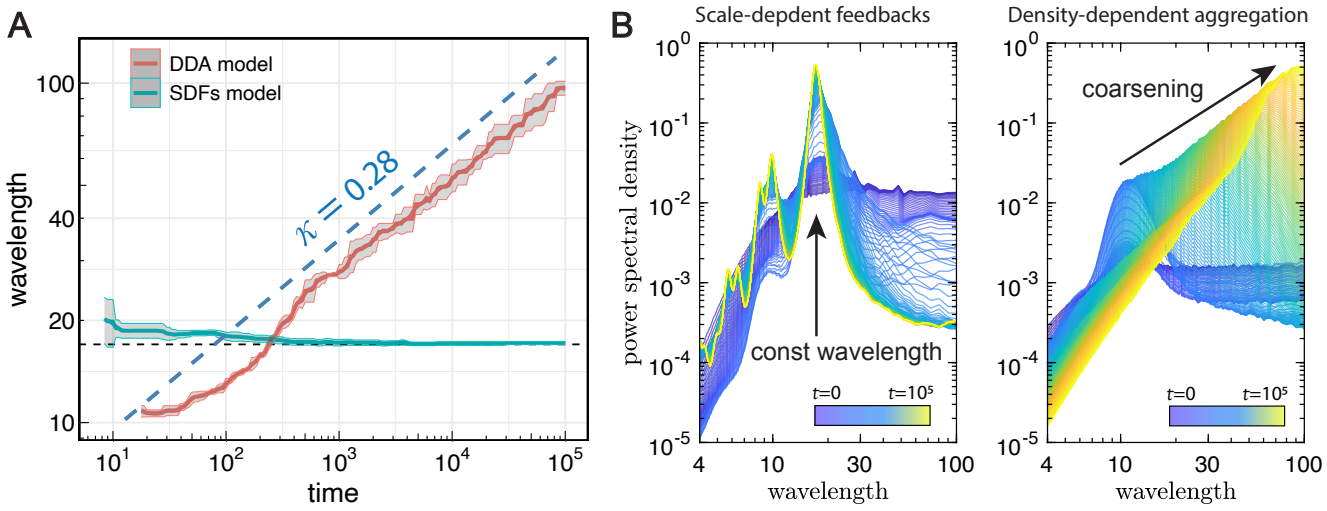

Fig. S12. (A) Scaling behavior of the pattern coarsening from the density-dependent aggregation (DDA) model, whereas lacking a coarsening behavior in the classic scale-dependent feedbacks (SDFs) model. Dashed line depicts the fitted function as $\ell \propto t^{\kappa}$ with exponent of 0.28. Lines represent the mean trend and bands of the SD from 10 independent realizations. (B) The power-spectrum density of SDFs and DDA models with consecutive time. The dominant peaks reveal a characteristic length scale of spatial patterns used in panel (A).

Movie S1. Dynamic behavior of spatial patterns results from scale-dependent feedback model Eqs.(8-9), where stationary patterns with saturated wavelength emerge for a long temporal evolution.

Movie S2. Dynamic behavior of spatial patterns results from the density-dependent aggregation model (Eq. 3), where the wavelength of patterns are unstable and coarsening with the temporal evolution.

Movie S3. The spatial dynamic behavior and spinodal bifurcation of phase-separation patterns within the ($\langle\tau\rangle$, δ)-parameter space.

References

1. J. Halatek and E. Frey. Rethinking pattern formation in reaction–diffusion systems. *Nature Physics*, 14(5):507–514, 2018.
2. F. Brauns, Jacob Halatek, and Erwin Frey. Phase-space geometry of reaction–diffusion dynamics. *Phy. Rev. X*, 10:041036, 2020.
3. R. Samuelson, Zachary Singer, and Jasper Weinburd. Advection and Autocatalysis as Organizing Principles for Banded Vegetation Patterns. *Journal of Nonlinear Science*, 29(1):255–285, 2019.
4. M. C. Cross and P. C. Hohenberg. Pattern formation outside of equilibrium. *Rev. Mod. Phys.*, 65:851–1112, 1993.
5. James D. Murray. *Mathematical Biology: I . An Introduction, Third Edition*, 2002.
6. L. A. Segel and Julius L. Jackson. Dissipative structure: An explanation and an ecological example. *Journal of Theoretical Biology*, 37(3):545–559, 1972.
7. L. Edelstein-Keshet. *Mathematical models in biology*. McGraw-Hill, New York, 1988.
8. Johan van de Koppel and Caitlin Mullan Crain. Scale-dependent inhibition drives regular tussock spacing in a freshwater marsh. *The American naturalist*, 168(5):136–47, 2006.
29. Christopher A. Klausmeier. Regular and irregular patterns in semiarid vegetation. *Science*, 284 (5421):1826–8, 1999.
10. Johan van de Koppel, Joanna C. Gascoigne, Guy Theraulaz, Max Rietkerk, Wolf M. Mooij, and Peter M. J. Herman. Experimental evidence for spatial self-organization and its emergent effects in mussel bed ecosystems. *Science*, 322(5902):739–742, 2008.
11. Max Rietkerk, Maarten C Boerlijst, Frank Van Langevelde, Reinier Hillerislambers, Johan Van, De Koppel, Lalit Kumar, Herbert H T Prins, and M De Roos. Self-organization of vegetation in arid Ecosystems. *The American naturalist*, 160(4):524–530, 2002.
12. Y. Mori, Alexandra Jilkine, and Leah Edelstein-Keshet. Wave-pinning and cell polarity from a bistable reaction-diffusion system. *Biophysical Journal*, 94(9):3684–3697, 2008.
13. Nicolas Verschueren and Alan Champneys. A Model for cell polarization without mass conservation. *SIAM J. Applied Dynamical Systems*, 16(4):1797–1830, 2017.
14. J. C. Maxwell. On the dynamical evidence of the molecular constitution of bodies. *Nature*, 11: 357–359, 1875.
15. Ehud Meron. *Nonlinear Physics of Ecosystems*. CRC Press, Boca Raton (FL; USA), 2015.
16. I. Noy-Meir. Stability of grazing systems: an application of predator-prey graphs. *Journal of Ecology*, 63(2):459–481, 1975.

17. Robert M May. Thresholds and breakpoints in ecosystems with a multiplicity of stable states. *Nature*, 269:471–477, 1977.
18. Johan van de Koppel, Max Rietkerk, Frank van Langevelde, Lalit Kumar, Christopher A Klausmeier, John M Fryxell, John W Hearne, Jelte van Andel, Nico de Ridder, Andrew K. Skidmore, Leo Stroosnijder, and Herbert H.T. Prins. Spatial heterogeneity and irreversible vegetation change in semiarid grazing systems. *The American naturalist*, 159(2):209–218, 2002.
19. Gertrud Berg, Peter Esselink, Menko Groeneweg, and Kathrin Kiehl. Micropatterns in Festuca rubra-dominated salt-marsh vegetation induced by sheep grazing. *Plant Ecology*, 132(1):1–14, 1997.
20. William F. Smith and Javad Hashemi. *Foundations of materials science and engineering*. McGraw-Hill series in materials science. McGraw-Hill, Boston, 4th edition, 2006.
21. Johan van de Koppel, Max Rietkerk, Norbert Dankers, and Peter M J Herman. Scale-dependent feedback and regular spatial patterns in young mussel beds. *The American naturalist*, 165(3): 66–77, 2005.
22. Ralf B. Bergmann and Andreas Bill. On the origin of logarithmic-normal distributions: An analytical derivation, and its application to nucleation and growth processes. *Journal of Crystal Growth*, 310(13):3135–3138, 2008.
23. M. Kahlweit. Ostwald ripening of precipitates. *Advances in Colloid and Interface Science*, 5(1): 1–35, 1975.
24. A. J. Bray and C. L. Emmott. Lifshitz-slyozov scaling for late-stage coarsening with an order-parameter-dependent mobility. *Phys. Rev. B*, 52:R685–R688, 1995.
25. I. M. Lifshitz and V V Slyosov. The kinetics of precipitation from supersaturated solid solutions. *J. Phys. Chem. Solids*, 19(1):35–50, 1961.
26. Murat Tiryakioğlu, Giray Ökten, David Hudak, Ralph T. Shuey, and Jaakko P. Suni. On evaluating fit of the lifshitz–slyozov–wagner (LSW) distribution to particle size data. *Materials Science and Engineering: A*, 527(6):1636–1639, 2010.
27. Murat Tiryakioğlu, Giray Ökten, and David Hudak. Statistics for estimating the population average of a lifshitz–slyozov–wagner (LSW) distribution. *Journal of Materials Science*, 44(21): 5754–5759, 2009.
28. Eric-jan Wagenmakers and Simon Farrell. AIC model selection using Akaike weights. *Psychonomic Bulletin and Review*, 11(1):192–196, 2004.
29. Christopher A. Klausmeier. Regular and irregular patterns in semiarid vegetation. *Science*, 284 (1):1826–1828, 1999.
30. J. von Hardenberg, A. Y. Kletter, H. Yizhaq, J. Nathan and E. Meron, Periodic versus scale-free patterns in dryland vegetation. *Proc. Roy. Soc. Biol. Sci.*, 277(1):1771–1776, 2010.
31. Anyuan Li, N. Matsuoka F. Niu, J. Chen, Z. Ge, W. Hu, D. Li, B. Hallet, J. van de Koppel, N. Goldenfeld, Q.-X. Liu. Ice needles weave patterns of stones in freezing landscapes. *Proc Natl Acad Sci USA*, 118(40):e2110670118, 2021.
32. Zhenpeng Ge, Quan-Xing Liu. Foraging behaviours lead to spatiotemporal self-similar dynamics in grazing ecosystems. *Ecology Letters*, 25(2):378-390, 2022.